

Bundle Adjusted Gaussian Avatars Deblurring

Muyao Niu^{1,2,*} Yifan Zhan^{1,2} Qingtian Zhu² Zhuoxiao Li² Wei Wang¹
Zhihang Zhong^{1,†} Xiao Sun^{1,†} Yinqiang Zheng²

¹Shanghai Artificial Intelligence Laboratory ²The University of Tokyo

Abstract

The development of 3D human avatars from multi-view videos represents a significant yet challenging task in the field. Recent advancements, including 3D Gaussian Splattings (3DGS), have markedly progressed this domain. Nonetheless, existing techniques necessitate the use of high-quality sharp images, which are often impractical to obtain in real-world settings due to variations in human motion speed and intensity. In this study, we attempt to explore deriving sharp intrinsic 3D human Gaussian avatars from blurry video footage in an end-to-end manner. Our approach encompasses a 3D-aware, physics-oriented model of blur formation attributable to human movement, coupled with a 3D human motion model to clarify ambiguities found in motion-induced blurry images. This methodology facilitates the concurrent learning of avatar model parameters and the refinement of sub-frame motion parameters from a coarse initialization. We have established benchmarks for this task through a synthetic dataset derived from existing multi-view captures, alongside a real-captured dataset acquired through a 360-degree synchronous hybrid-exposure camera system. Comprehensive evaluations demonstrate that our model surpasses existing baselines.

1. Introduction

Motion blur manifests in images when changes in the scene occur during the exposure period of the camera. Unlike specific applications such as time-lapse photography [47, 55], motion blur is typically regarded as an undesirable effect that significantly diminishes the perceptual quality of images. Despite advancements in camera technology, motion blur remains a common issue due to unpredictable and varying scene dynamics. Consequently, a plethora of algorithms has been devised for the post-processing of blurry images and videos. These methods seek to reconstruct clear and

sharp visual details from degraded observations [4, 14, 15, 28, 35, 42, 43, 54, 58, 61, 65, 65, 66, 68, 72, 77–80].

In the realm of 3D reconstruction, the creation of high-quality 3D human avatars holds immense potential for industries such as gaming, augmented and virtual reality (AR/VR), and film production. Recent innovations have established the viability of deriving 3D human avatars from videos captured from limited viewpoints [10, 11, 16, 17, 19, 44, 50–52, 59, 64, 67, 67, 69] and even single images [5, 12, 36, 75]. Moreover, recent methods that employ 3D Gaussian Splattings [20] and the Skinned Multi-Person Linear model (SMPL) [38] have achieved notable success. These techniques are distinguished by their superior performance and computational efficiency. Typically, these methods rely on video data obtained from static cameras, utilizing the SMPL parameters to calibrate each frame based on the dynamic human videos captured from multiple views.

While these models achieve remarkable outcomes with well-calibrated and high-quality video frames, their performance can be substantially compromised by blur effects resulting from human motion. In practical settings, such motion-induced blur is often unavoidable, given the unpredictable speeds and movements of the subjects. This variability poses significant challenges in preserving the visual quality of the captured images, thereby affecting the fidelity of the 3D reconstructions.

In particular, blur effects may detrimentally impact the performance of existing human avatar models in two distinct ways. First, blurry captures can lead the 3DGS model to learn a distorted 3D representation, stemming from the intrinsic ambiguity of motion blur (Fig. 1). This ambiguity hampers the accurate recovery of structural information and texture details. Second, despite the possibility of calibrating static cameras prior to capturing, as demonstrated in prior research, blurred captures still result in erroneous estimation of SMPL parameters¹.

A pragmatic strategy to mitigate this issue involves im-

^{*}This work was done during the author’s internship at the Shanghai Artificial Intelligence Laboratory.

[†]Corresponding authors.

¹Certain studies, such as [11], have incorporated a correction module to refine pose parameters during training. Nevertheless, experimental results reveal that these modifications often do not achieve optimal performance due to the lack of a precise formulation for the blur process.

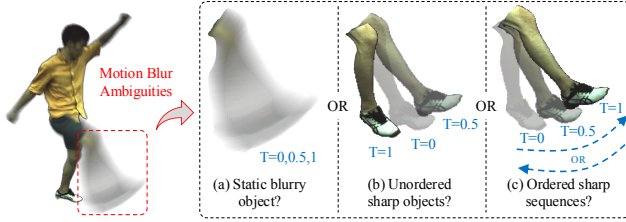


Figure 1. **The ambiguity brought by motion blur.** When reconstructing sharp 3DGS avatars from blurry frames, motion-induced blur introduces challenging ambiguities in motion interpretation.

plementing a two-stage baseline approach. Initially, 2D deblurring techniques [35, 46, 73, 79] are employed to restore sharp video sequences. Subsequently, the deblurred frames are utilized to train the 3DGS avatar model. While this baseline method enhances the visual quality by partially resolving the motion blur ambiguity through 2D deblurring, it overlooks the intrinsic 3D scene information. This oversight often results in inconsistencies across multiple views during the deblurring process, which can compromise the effectiveness of the 3DGS model training and lead to sub-optimal performance outcomes.

To tackle these challenges, we introduce the first method capable of reconstructing sharp, animatable 3D human avatars directly from blurry video frames. Leveraging the distinctive properties of human avatar models, we extend the conventional physics-based 2D image blur process into a 3D-aware blur formation model. This novel approach decomposes the inherently ill-posed deblurring problem into two essential tasks: optimizing sub-frame motion representations and constructing the canonical sharp 3DGS avatar model. To resolve the sub-frame motion ambiguity introduced by motion-induced blur, we propose a 3D-aware human motion model based on the SMPL framework. This model facilitates the simultaneous recovery of plausible sub-frame motion for each blurry frame alongside the reconstruction of the sharp 3DGS avatar model. By utilizing the optimized motion and canonical 3DGS, we synthesize motion-blurred frames through the averaging of a sequence of virtual sharp images and compute the loss in comparison to the corresponding “ground-truth” blurry frames.

As there are currently no benchmarks for evaluating this task, we have developed a synthetic dataset based on the widely-used ZJU-MoCap dataset [50], complemented by a real-captured dataset obtained through a 360-degree hybrid-exposure camera system. Comprehensive evaluations confirm the superiority of our approach. The codes and dataset are available to the public for future work in this field. Our contributions can be summarized as follows:

- We introduce the first method designed to reconstruct sharp, animatable 3D human avatars from blurry RGB videos. Our approach, underpinned by a physics-based

3D-aware blur formation model, enables the concurrent estimation of sub-frame motion and reconstruction of sharp 3DGS human avatars.

- To establish a benchmark for this task, we offer both a synthetic dataset derived from the ZJU-MoCap dataset and a real dataset captured using a 360-degree hybrid-exposure camera system.
- Our method demonstrates significant enhancements in removing motion blur and reconstructing high-quality human avatars, surpassing existing baselines.

2. Related Work

2.1. Image & Video Deblurring

In recent years, the deblurring paradigm has shifted from traditional methods centered on blur kernel estimation [14, 28, 54, 68] to learning-based approaches that directly regress sharp images [25, 42, 58, 61, 65, 72, 77–79]. Various network architectures [15, 43, 66, 77, 80] have been extensively explored for deblurring tasks. The adoption of deformable convolution [6, 81], as demonstrated in [65], has enhanced performance by aligning neighboring blurry frames. Additionally, techniques incorporating optical flow for precise motion compensation, as in [45] and [56], have been explored. GANs, used by [24, 25], focus on improving perceptual image quality in deblurring. Transformers have also gained traction in low-level vision tasks [33], with models like Restormer [73], RVRT [34], and VDTR [3] showing strong performance in deblurring. Recently, the advent of 3D technologies such as NeRF [40] and 3DGS [20] has promoted exploration into leveraging multi-view information for enhanced deblurring [2, 26, 39, 57, 60, 63, 76]. Specifically, methods like [26, 39, 63, 76] focus on deblurring static scenes affected by defocus or camera movement, while some approaches [2, 57, 60] address the complexities of deblurring dynamic scenes with motion blur caused by both camera and scene movement. In contrast, we focus on reconstructing animatable 3D human avatars using captures from static multi-view cameras, thus it is important to leverage prior knowledge of human body, such as the SMPL model [38].

In recent years, deblurring has shifted from traditional blur kernel estimation [14, 28, 54, 68] to learning-based methods that directly predict sharp images [25, 42, 58, 61, 65, 72, 77–79]. Various network architectures [15, 43, 66, 77, 80] have been extensively explored for deblurring tasks. The adoption of deformable convolution [6, 81], as demonstrated in [65], has enhanced performance by aligning neighboring blurry frames. Additionally, techniques incorporating optical flow for precise motion compensation, as in [45] and [56], have been explored. GANs, used by [24, 25], focus on improving perceptual image quality in deblurring. Transformers have also gained traction in low-

level vision tasks [33], with models like Restormer [73], RVRT [34], and VDTR [3] showing strong performance in deblurring. Recently, the advent of 3D technologies such as NeRF [40] and 3DGS [20] has also promoted exploration into leveraging multi-view information for enhanced deblurring [2, 26, 39, 57, 60, 63, 76]. Specifically, methods like [26, 39, 63, 76] focus on deblurring static scenes affected by defocus or camera movement, while some approaches [2, 57, 60] address the complexities of deblurring dynamic scenes with blur caused by both camera and scene movement. In contrast, we focus on reconstructing animatable 3D human avatars using captures from static multi-view cameras.

2.2. 3D Human Avatars

Since the groundbreaking introduction of Neural Radiance Fields (NeRFs) [40], there has been a significant surge in research on neural rendering for human avatars. Most studies focus either on learning a human-related encodings [44, 59, 69], or on developing a canonical NeRF representation where camera rays are warped from the observation space [9, 18, 19, 31, 49, 51, 64, 67, 71]. Recently, 3D Gaussian Splatting (3DGS) [20] has revolutionized the field by modeling the rendering process as the splatting of 3D Gaussians. The superior performance of 3DGS in both quality and speed has spurred extensive research into using 3D Gaussian representations for dynamic human reconstruction [10, 11, 16, 23, 27, 32, 37, 41, 52, 70, 82]. [52] learns a non-rigid deformation network to reconstruct animatable clothed human avatars and introduces isometric regularization on both the Gaussian mean vectors and the covariance matrices. [10] explicitly represents humans with animatable 3D Gaussians and further augments the model with dynamic properties to support pose-dependent appearance modeling. [11] encodes Gaussian Splatting in the canonical space and transforms 3D Gaussians to the posed space using Linear Blend Skinning (LBS). To enable fast optimization, they further operate on 3D Gaussians using 3D human priors and Kullback–Leibler (KL) divergence guidance. However, these methods rely on high-quality images, which can be challenging to capture due to the varying movement speeds of the subject. In this paper, we propose to model the physics-based blur formation process caused by human motion, and simultaneously optimize human motion and sharp 3DGS avatars from blurry observations.

3. Preliminary

3.1. SMPL

SMPL (Skinned Multi-Person Linear) model [38] is a parametric human body model that represents the 3D geometry of the human body based on shape, pose, and Linear Blend Skinning (LBS) weight parameters. Specifically, the SMPL

model represents the human body as a triangulated mesh $\mathbf{M}(\beta, \Theta)$ with a fixed topology. The vertices $\mathbf{V} \in \mathbb{R}^{6890 \times 3}$ of the mesh are generated as a function of the shape β , pose Θ , and LBS weights \mathcal{B} :

$$\mathbf{V} = W(\mathbf{T}_P(\beta, \Theta), J(\beta), \Theta, \mathcal{B}), \quad (1)$$

where $W(\cdot)$ represents the Linear Blend Skinning (LBS) function, $\mathbf{T}_P(\beta, \Theta) \in \mathbb{R}^{6890 \times 3}$ is the rest pose template mesh, $J(\beta) \in \mathbb{R}^{24 \times 3}$ are the joint locations.

Based on the SMPL model [38], we can transfer a 3D point in the canonical space to the observation space. For example, 3D point \mathbf{p}^c in the canonical space can be transformed to the observation space \mathbf{p}^o as:

$$\mathbf{p}^o = \sum_{k=1}^K w_k (\mathbf{G}_k(J(\beta), \Theta) \mathbf{p}^c + \mathbf{b}_k(J(\beta), \Theta, \beta)), \quad (2)$$

where $\mathbf{G}_k(J(\beta), \Theta)$ and $\mathbf{b}_k(J(\beta), \Theta, \beta)$ are the transformation matrix and translation vector of joint k respectively, w_k is the corresponding LBS weights.

3.2. 3D Gaussian Splattings (3DGS)

3D Gaussian Splattings (3DGS) [20] represents a 3D scene with a set of unstructured discrete 3D Gaussians. Each 3D Gaussian is defined with a center point \mathbf{p} and a 3D covariance matrix Σ in world space, given by:

$$G(\mathbf{x}) = \frac{1}{(2\pi)^{3/2} |\Sigma|^{1/2}} e^{-\frac{1}{2}(\mathbf{x}-\mathbf{p})^\top \Sigma^{-1}(\mathbf{x}-\mathbf{p})}. \quad (3)$$

To ensure the positive semi-definiteness of the 3D covariance matrix Σ , it is decomposed into two learnable components: a quaternion $\mathbf{R} \in \mathbb{R}^4$ representing rotation and a vector $\mathbf{S} \in \mathbb{R}^3$ representing scaling. The covariance matrix is then defined as:

$$\Sigma = \mathbf{R} \mathbf{S} \mathbf{S}^\top \mathbf{R}^\top. \quad (4)$$

To project 3D Gaussians onto a 2D screen space, they are first transformed from world to ray coordinates using the world-to-camera transformation matrix \mathbf{W} :

$$G(\mathbf{x}) = \frac{1}{(2\pi)^{3/2} |\Sigma'|^{1/2}} e^{-\frac{1}{2}(\mathbf{x}-\mathbf{p}')^\top \Sigma'^{-1}(\mathbf{x}-\mathbf{p}')}, \quad (5)$$

where $\mathbf{p}' = \mathbf{m}(\mathbf{W}\mathbf{p} + \mathbf{d})$ and $\Sigma' = \mathbf{J}\mathbf{W}\Sigma\mathbf{W}^\top\mathbf{J}^\top$. Here, $\mathbf{m}(\cdot)$ denotes the mapping from camera to ray coordinates.

After projecting 3D Gaussians onto the 2D screen, the overlapping 2D Gaussians in each pixel are counted, and their color c_i and density α_i contributions are calculated. The pixel color is then obtained by blending N ordered Gaussians:

$$\hat{C} = \sum_{i \in N} c_i \alpha_i \prod_{j=1}^{i-1} (1 - \alpha_j). \quad (6)$$

Adaptive control is employed to improve rendering quality, which includes three operations: split, clone, and prune. Splitting and cloning are applied to large Gaussians if the scaling magnitude exceeds a threshold, while pruning eliminates Gaussians with excessively small opacity (α) or large scaling magnitudes.

In our method, 3D Gaussians are initialized from the SMPL model, *i.e.*, the mean of each 6890 Gaussians are initialized from the 3D coordinates of the 6890 points defined by the SMPL model.

4. Method

In this section, we elaborate on the specifics of our model. Utilizing motion-induced blurry videos captured by static cameras, our model concurrently estimates sub-frame motion and reconstructs sharp 3DGS human avatars.

4.1. 3D Blur Formation Model

The physical mechanism of image formation involves capturing photons during the camera’s exposure period and converting them into electrical signals. This process can be mathematically described in the 2D camera coordinate space as the integration of virtual sharp images over the exposure duration:

$$\mathbf{I}^B(\mathbf{u}) = \phi \int_0^\tau \mathbf{I}_t^S(\mathbf{u}) dt, \quad (7)$$

where $\mathbf{I}^B(\mathbf{u}) \in \mathbb{R}^{3 \times H \times W}$ denotes the captured blurry image, with H and W representing the image’s height and width, respectively. The term $\mathbf{u} \in \mathbb{R}^2$ specifies the pixel location, ϕ is a normalization factor, τ is the exposure time, and $\mathbf{I}_t^S(\mathbf{u}) \in \mathbb{R}^{3 \times H \times W}$ is the virtual sharp image at a specific time t within the exposure period.

This continuous integration process can be discretely approximated by:

$$\mathbf{I}^B(\mathbf{u}) \approx \frac{1}{n} \sum_{i=0}^{n-1} \mathbf{I}_i^S(\mathbf{u}), \quad (8)$$

where the blurred image $\mathbf{I}^B(\mathbf{u})$ is estimated by averaging n virtual intermediate sharp images $\mathbf{I}_i^S(\mathbf{u})$.

Here we redefine the blur formation process from the perspective of 3D human avatar modeling, expanding it beyond the confines of the 2D camera coordinate space. Specifically, we model the motion of a 3DGS avatar during the exposure time using a set of K 3D Gaussians $\{G_k(\mathbf{x})\}_{k=0}^{K-1}$ located in the canonical space, accompanied by a sequence of T SMPL [38] parameters $\{\mathcal{S}_t\}_{t=0}^{T-1} = \{\Theta_t, \beta_t, \mathcal{B}_t\}_{t=0}^{T-1}$. These parameters dynamically warp the 3D Gaussians into the observation space at each discrete time step t . Consequently, the resultant blurry image, \mathbf{I}^B ,

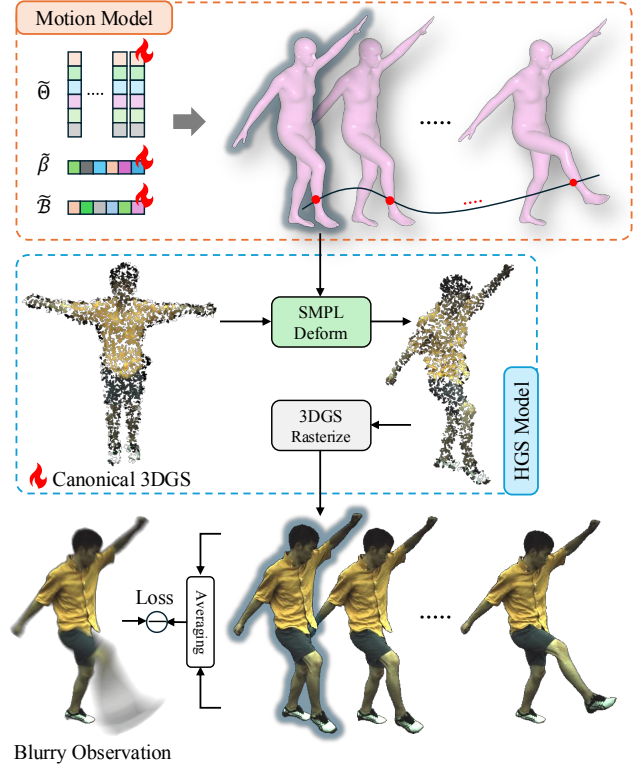


Figure 2. **Brief illustration of the pipeline.** For a set of motion-blurred images, we construct an animatable 3DGS avatar to represent the 3D scene. We model the sub-frame motion for each blurry frame based on SMPL model, then warp the canonical 3DGS based on the estimated motion parameters. The final blurry image is generated by averaging these virtual sharp images, effectively capturing the motion blur within the scene.

can be modeled as:

$$\mathbf{I}^B = \frac{1}{T} \sum_{t=0}^{T-1} \mathcal{R}(\mathcal{W}(\{G_k(\mathbf{x})\}_{k=0}^{K-1}, \mathcal{S}_t), \mathbf{R}, \mathbf{K}), \quad (9)$$

where \mathbf{x} denotes the coordinates of the 3D Gaussians, \mathbf{R} and \mathbf{K} signify the camera’s extrinsic and intrinsic parameters, respectively. Here, \mathcal{R} represents the rasterization process of the 3DGS model, and \mathcal{W} refers to the warping of 3D Gaussians from the canonical space to the observation space, governed by the SMPL parameters \mathcal{S}_t .

4.2. 3D Human Motion Model

As depicted in Fig. 1, motion-induced blur generates significant ambiguities in motion, which are evident in the pixel space. The resolution of this ill-posed problem hinges on accurately estimating plausible sub-frame motion during the exposure period. To address this challenge, we have developed a 3D-aware human motion model that effectively estimates the sub-frame motion for each exposure period as well as the plausible inter-frame global motion.

4.2.1 Pose parameters

Sub-frame rigid sequential pose model. The pose parameters Θ_t , defined within the SMPL model as $\Theta_t \in \mathbb{R}^{24 \times 3}$, describe the rotations of 24 joints at each time step t , represented in the group $\mathbf{SO}(3)$. Given the inherent continuity of joint motion, we employ the De Boor-Cox formulation for B-Splines [7, 30, 53, 62] to interpolate intermediate poses.

For each joint j within the SMPL model, we define P learnable control parameters $\tilde{\Theta}^j = \{\tilde{\Theta}_p^j\}_{p=0}^{P-1} \in \mathbb{R}^{P \times 3}$, where P is the pre-defined number of control knots. At each time step t , the interpolation process begins with the computation of the unified timestep basis $\mathbf{B}(t) \in \mathbb{R}^{1 \times P}$:

$$\mathbf{B}(t) = [1, \frac{t}{T}, (\frac{t}{T})^2, \dots, (\frac{t}{T})^{P-1}], \quad (10)$$

where T is the total exposure time. Using this basis, the interpolated pose parameters for the j -th joint at time step t are determined by:

$$\hat{\Theta}_t^j = \mathbf{B}(t) \cdot \mathcal{M}^P \cdot \tilde{\Theta}^j, \quad (11)$$

where $\mathcal{M}^P \in \mathbb{R}^{P \times P}$ is the general interpolation matrix [53], defined as:

$$\mathcal{M}_{i,j}^P = C_{P-1-i}^{P-1} \sum_{s=j}^{P-1} (-1)^{s-j} C_{s-j}^P (P-s-1)^{P-1-i}, \quad (12)$$

with $C_k^n = \frac{n!}{k!(n-k)!}$ denoting the binomial coefficient.

Non-rigid pose deformation model. Although B-Spline interpolation is adept at capturing basic pose trajectories, it is somewhat limited in expressing more complex, high-frequency pose variations. To surmount this limitation, we incorporate a non-rigid pose displacement Δ_t^j for each joint j at each time step t within the exposure period:

$$\Delta_t^j = G_{disp}(\hat{\Theta}_t^j; \theta_{disp}), \quad (13)$$

$$\Theta_t^j = \hat{\Theta}_t^j + \Delta_t^j, \quad (14)$$

where G_{disp} denotes the non-rigid deformation network tailored to account for nuanced pose variations, and θ_{disp} represents its set of learnable parameters. This methodology enables our model to more accurately capture intricate pose dynamics, thereby providing a more realistic representation of motion within each blurred frame.

Inter-frame motion regularization. While using L1 loss can provide satisfactory photometric results at the middle timestep of the exposure period ($t = 0.5$), it may encounter directional ambiguity, as illustrated in Fig. 1(c). This ambiguity arises because either direction of motion might produce a similarly plausible blurry image, leading to potential inaccuracies in motion direction estimates and consequently, misaligned renderings at non-middle timesteps.

To address this challenge, we introduce a regularization term based on the inter-frame continuity typically observed in video sequences. It measures the L2-distance between the pose parameters at the final timestep of the current exposure period and those at the initial timestep of the subsequent exposure period:

$$\mathcal{L}_{reg} = \frac{1}{24 \cdot (N_e - 1)} \sum_{n=0}^{N_e-2} \sum_{j=0}^{23} \|\hat{\Theta}_{n,T-1}^j - \hat{\Theta}_{n+1,0}^j\|_2, \quad (15)$$

where $\hat{\Theta}_{t,n}^j$ denotes the estimated pose parameters of the j -th joint at timestep t for the n -th exposure period.

This regularization term aims to enhance the coherence of joint movements between consecutive frames, ensuring that the motion is consistent and logically progresses from one frame to the next.

4.2.2 Shape Parameters

We optimize a single shared shape parameter $\hat{\beta} \in \mathbb{R}^{10}$ across all time steps during the training phase. This decision is predicated on the intuitive understanding that a person’s shape remains consistent throughout a motion sequence.

4.2.3 Linear Blend Skinning (LBS) weights

The SMPL model [38] includes pre-trained LBS weights, denoted as $\tilde{\mathcal{B}}$. In alignment with prior works, we utilize the same LBS weights, $\tilde{\mathcal{B}}$ across all time steps. We begin with the initial pre-trained SMPL weights and refine them during the training process by introducing an LBS offset δ :

$$\hat{\mathcal{B}} = \tilde{\mathcal{B}} + \delta, \quad (16)$$

where δ is computed by a deformation estimation network. This network processes the coordinates of all 3D Gaussians, facilitating dynamic adjustments to the LBS weights.

4.3. Optimization

Pipeline. The optimization pipeline of our model is illustrated in Fig. 2. The first step involves estimating the sub-frame motion using our dedicated motion model. Following this, the canonical 3D Gaussian Splatting (3DGS) model is transformed based on the estimated motion parameters. Subsequently, sharp virtual images are synthesized for each intermediate timestep. These images are then collectively averaged to mimic the physical process of motion blur, generating the final blurry image for loss calculation.

Loss function. Our loss function includes the L1 photometric loss, which measures the difference between the synthesized blurry frame $\hat{\mathbf{I}}^B$ and the “ground-truth” blurry frame \mathbf{I}^B , combined with the inter-frame motion regularization loss:

$$\mathcal{L}_{pho} = \|\hat{\mathbf{I}}^B - \mathbf{I}^B\| + \mathcal{L}_{reg}. \quad (17)$$

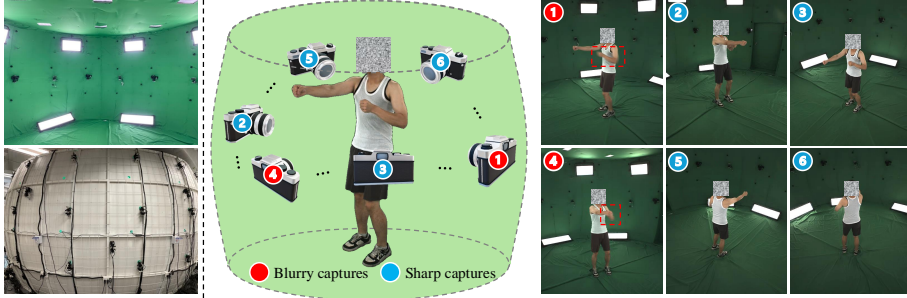


Figure 3. **Camera system for real data capture.** (a) The inner side and outer side of the capture cage. (b) Demonstration of the multi-view camera system and the corresponding captured images. Only part of the views are shown in the figure.

Type	Blur	Sharp
View Num.	4	8
Exposure (ms)	50	3.125
Resolution	2448 × 2048	
Camera	BFS-U3-51S5C	
FPS	15	
Scene Num.	8	
Format	PNG	

Table 1. **Configuration of the captured real data.** The blurry captures and the sharp captures are synchronized.

Table 2. **Quantitative comparisons on synthetic dataset.** We color each result as **best**, **second best**, and **third best**.

Methods	PSNR ↑	SSIM ↑	LPIPS ↓
GauHuman [11]	23.080	0.7660	0.2277
ShiftNet [29] + GauHuman	23.089	0.7695	0.2219
RVRT [34] + GauHuman	23.078	0.7697	0.2218
VRT [35] + GauHuman	23.074	0.7696	0.2205
BSST [74] + GauHuman	23.081	0.7698	0.2212
Ours	25.546	0.8290	0.1476

Table 3. **Quantitative comparisons on real dataset.** We color each result as **best**, **second best**, and **third best**.

Methods	PSNR ↑	SSIM ↑	LPIPS ↓
GauHuman [11]	25.602	0.8044	0.2380
ShiftNet [29] + GauHuman	25.549	0.8043	0.2347
RVRT [34] + GauHuman	25.547	0.8065	0.2343
VRT [35] + GauHuman	25.553	0.8067	0.2345
BSST [74] + GauHuman	25.568	0.8068	0.2342
Ours	27.010	0.8271	0.1668

The total loss ensures that the model learns to generate realistic motion while closely matching the observed blurry frames.

5. Experiments

5.1. Datasets

Evaluating blur-aware 3D human avatar techniques requires datasets that provide multi-view images with motion-induced blur distortions along with their corresponding sharp ground truth images. Since no datasets currently meet these criteria, we contribute both a synthetic dataset and a real-captured dataset to establish a benchmark for this task.

Synthetic dataset. We create our synthetic dataset based on the ZJU-MoCap [50] dataset, a widely used dataset for evaluating 3D human avatar techniques. Consistent with previous works [8, 11, 52, 67], we select six human subjects (IDs: 377, 386, 387, 392, 393, 394) for our experiments. To generate blurry video frames, we average $K_{blur} = 5$ consecutive sharp frames to synthesize 50 blurry frames per camera. To reduce discontinuities from direct averaging, we utilize the RIFE model [13] to interpolate eight intermediate frames between each pair of adjacent frames, then average these interpolated frames to create the final blurry frame. For training, we use the blurry frames from Cameras 04, 10, 16, and 22. For evaluation, we use the ground-truth sharp frames from the remaining 18 cameras, exclud-

ing Camera 03 due to its distinct appearance from the others. We calibrate the SMPL parameters using the blurry video frames with EasyMoCap [1, 50], and utilize Segment-Anything [22] to obtain segmentation masks.

Real dataset. To evaluate our model under realistic conditions, we collected a multi-view dataset consisting of real blurry videos with synchronous sharp videos from novel views. The multi-camera setup used for data collection features 12 time-synchronized Blackfly BFS-U3-51S5C cameras arranged in a 360-degree spatial configuration, as illustrated in Fig. 3. In each scene, four cameras capture blurry videos, while the remaining eight record sharp videos for novel-view evaluation. The exposure time for the cameras capturing blurry videos is set 16 times longer than that for the sharp video cameras. To maintain consistent pixel intensity between blurry and sharp videos, the blurry cameras are equipped with a 1/16 ND filter. Videos are recorded at a resolution of 2080 × 2048 with a frame rate of 15 FPS. Further details of the dataset configuration are summarized in Tab. 1. Similar to our synthetic dataset, we calibrate SMPL parameters using EasyMoCap [1] and generate segmentation masks with Segment-Anything [22]. Additional information is provided in the supplementary material.

5.2. Implementation Details

Our model is implemented using PyTorch [48]. Optimization is conducted with the Adam optimizer [21], configured

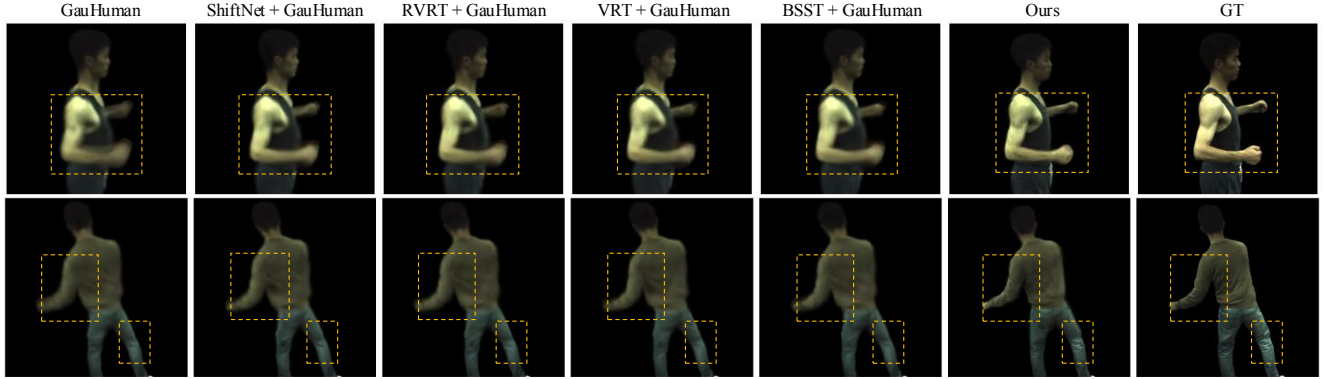


Figure 4. **Qualitative comparison on synthetic dataset.** Zoom in for the best view.

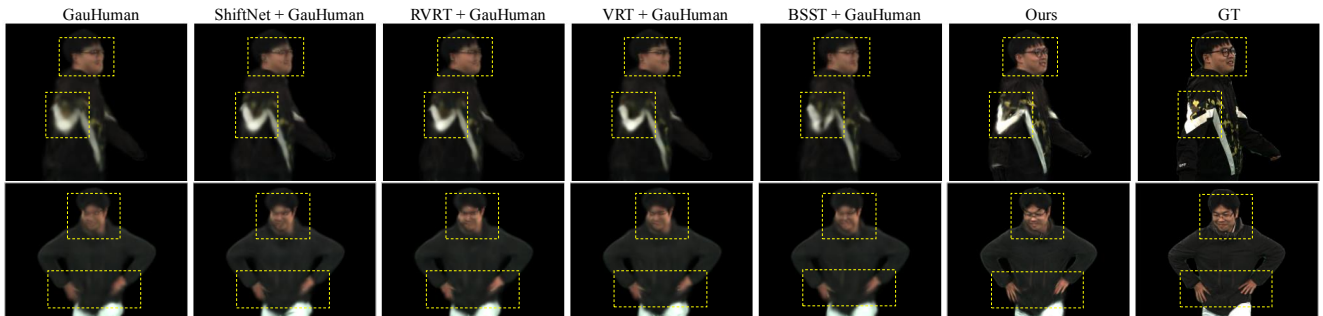


Figure 5. **Qualitative comparison results on real data.** Zoom in for the best view.

Table 4. **Quantitative ablation results on real dataset.** We color code result as **best**, **second best**, and **third best**.

Models	PSNR \uparrow	SSIM \uparrow	LPIPS \downarrow
w/o interp.	25.825	0.8140	0.1729
w/o non-rigid	26.426	0.8184	0.1743
w/o LBS opt.	26.821	0.8233	0.1697
w/o shape opt.	26.964	0.8261	0.1669
Ours (full model)	27.010	0.8271	0.1668

with $\beta_1 = 0.9$ and $\beta_2 = 0.999$. The learning rates and exponential decay settings are aligned with those in the original 3DGS framework [20]. Consistent with the approach in [11], we downsample the resolution to 512×512 for the synthetic dataset, while for the real dataset, we use a resolution of 612×512 . All models are trained on a single NVIDIA GeForce RTX 4090. Since the images contain extensive black areas, we crop each image according to the bounding box of the human for quantitative evaluation.

5.3. Comparisons

To assess the effectiveness of our method, we compared it against several baseline approaches. The simplest baseline involved training a 3DGS avatar model directly on blurry video frames using the state-of-the-art 3DGS human avatar model. Additionally, we evaluated two-stage methods that

Table 5. **Quantitative ablation results on synthetic dataset.** We color code result as **best**, **second best**, and **third best**.

Models	PSNR \uparrow	SSIM \uparrow	LPIPS \downarrow
w/o interp.	24.009	0.8053	0.1620
w/o non-rigid	25.301	0.8229	0.1545
w/o LBS opt.	25.394	0.8261	0.1486
w/o shape opt.	25.529	0.8284	0.1481
Ours (full model)	25.546	0.8290	0.1476

first apply 2D deblurring techniques such as RVRT [34] (NeurIPS 2022), ShiftNet [29] (CVPR 2023), VRT [35] (TIP 2024), and BSST [74] (CVPR 2024) to restore sharp images, followed by training a 3D human avatar model on these restored frames. Some recent approaches [26, 39, 63, 76] use multi-view information through NeRF or 3DGS to address deblurring. However, these methods are restricted to handling blur caused by camera motion or defocus, making them inapplicable to our task.

Quantitative results. Quantitative comparisons on the synthetic and real datasets are summarized in Tab. 2 and Tab. 3. The two-stage baselines yield sub-optimal results, with noticeably lower metrics. This outcome arises because these 2D deblurring models do not account for multi-view consistency across different viewpoints and lack modeling of

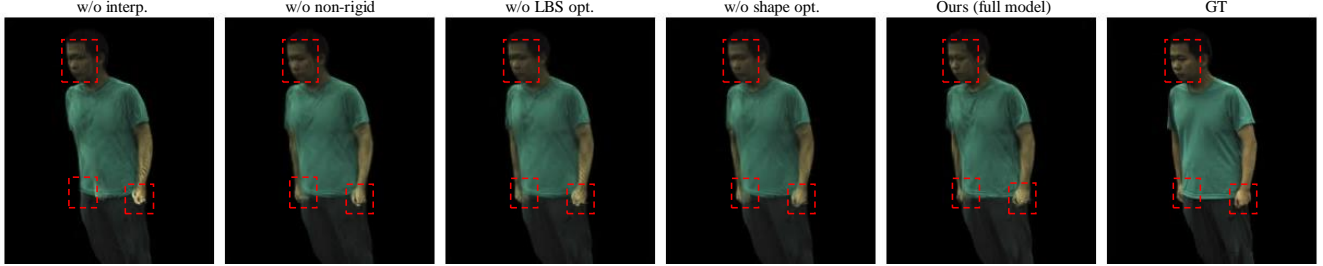


Figure 6. **Qualitative results for ablation studies.** Zoom in for the best view.

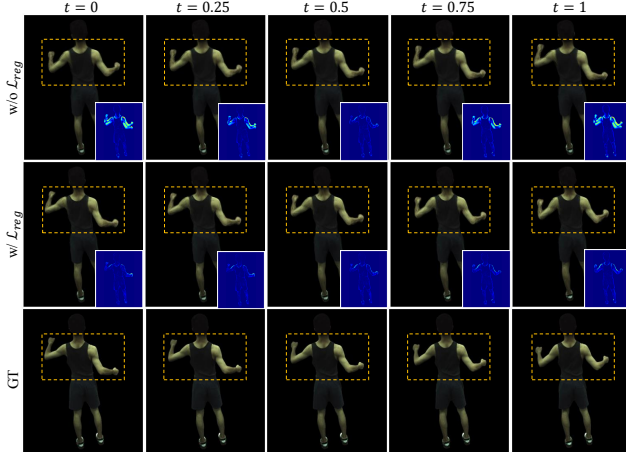


Figure 7. **Qualitative ablation results for \mathcal{L}_{reg} .** Model w/o \mathcal{L}_{reg} gives bad results for non-middle timesteps due to incorrect motion direction estimates. Zoom in for the best view.

the intrinsic 3D structure of the scene. In contrast, our method significantly outperforms these baselines across all metrics by integrating the motion-induced blur formation process and exploiting multi-view information from the video frames. Furthermore, the results indicate that the two-stage baselines only marginally outperform the direct 3DGS avatar methods, indicating that inconsistencies in deblurring across multiple views limit the 3DGS model’s capability to achieve satisfactory results.

Qualitative results. Qualitative comparisons between our method and other baselines are displayed in Fig. 4 and Fig. 5. While combining 2D deblurring techniques with the 3DGS avatar model yields slight improvements in reconstruction (e.g., in the arm region in Fig. 4), significant visual artifacts persist, such as residual blurriness and lack of detail around body edges. These issues stem from inconsistent deblurring across different views, as 2D deblurring methods fail to enforce multi-view consistency. In contrast, our approach incorporates the physics-based blur formation process directly into the model, enabling it to accurately learn the underlying 3D representation for simultaneous deblurring and avatar reconstruction. In addition, since our

Table 6. **Quantitative ablation results for \mathcal{L}_{reg} .** We mark **better** results for each sector.

K_{blur}	Models	Middle Timestep			Non-middle Timesteps		
		PSNR \uparrow	SSIM \uparrow	LPIPS \downarrow	PSNR \uparrow	SSIM \uparrow	LPIPS \downarrow
5	w/o \mathcal{L}_{reg}	25.567	0.8296	0.1478	24.421	0.8111	0.1601
	w/ \mathcal{L}_{reg}	25.546	0.8290	0.1476	25.417	0.8269	0.1485
7	w/o \mathcal{L}_{reg}	25.113	0.8197	0.1585	23.737	0.7950	0.1758
	w/ \mathcal{L}_{reg}	25.155	0.8200	0.1557	25.036	0.8179	0.1567
9	w/o \mathcal{L}_{reg}	24.628	0.8114	0.1680	23.198	0.7825	0.1888
	w/ \mathcal{L}_{reg}	24.680	0.8126	0.1636	24.605	0.8111	0.1645
11	w/o \mathcal{L}_{reg}	24.241	0.8009	0.1786	22.926	0.7717	0.1998
	w/ \mathcal{L}_{reg}	24.353	0.8039	0.1725	24.317	0.8031	0.1726

Table 7. **Quantitative results for different control knot number P and virtual sharp image number T .** We color code result as **best**, **second best**, and **third best** for each section.

P	PSNR \uparrow	SSIM \uparrow	LPIPS \downarrow	T	PSNR \uparrow	SSIM \uparrow	LPIPS \downarrow
2	25.516	0.8289	0.1480	3	25.528	0.8276	0.1503
3	25.482	0.8284	0.1485	5	25.546	0.8290	0.1476
4	25.546	0.8290	0.1476	7	25.532	0.8281	0.1499
5	25.540	0.8288	0.1490	9	25.522	0.8279	0.1501

method is able to recover the sub-frame motion, high frame-rate sharp videos could be further recovered.

5.4. Ablation Study

Model components. We performed ablation studies on various model components to assess our method’s design:

- Optimizing the pose independently for each timestep rather than using pose interpolation (w/o interp.).
- Using only the rigid sequential pose model, excluding non-rigid pose displacements (w/o non-rigid).
- Using pre-trained LBS weights without additional optimization (w/o LBS opt.).
- Employing calibrated SMPL shape parameters directly without further optimization (w/o shape opt.).

The quantitative and qualitative results are shown in Tab. 5, Tab. 4, and Fig. 6. Optimizing the pose for each intermediate timestep individually, instead of through interpolation, leads to inaccurate pose estimation and reduced

Table 8. **Quantitative comparison results with different K_{blur} .** We color code result as **best**, **second best**, and **third best**.

K_{blur}	Metrics	GauH	ShiftNet + GauH	RVRT + GauH	VRT + GauH	BSST + GauH	Ours
7	PSNR \uparrow	22.983	23.003	22.992	22.972	23.009	25.113
	SSIM \uparrow	0.7599	0.7648	0.7650	0.7654	0.7652	0.8197
	LPIPS \downarrow	0.2378	0.2314	0.2301	0.2299	0.2294	0.1585
9	PSNR \uparrow	22.693	22.699	22.692	22.693	22.732	24.628
	SSIM \uparrow	0.7532	0.7585	0.7587	0.7588	0.7590	0.8114
	LPIPS \downarrow	0.2497	0.2426	0.2411	0.2412	0.2409	0.1680
11	PSNR \uparrow	22.635	22.632	22.644	22.647	22.652	24.241
	SSIM \uparrow	0.7549	0.7554	0.7555	0.7564	0.7557	0.8009
	LPIPS \downarrow	0.2552	0.2502	0.2477	0.2480	0.2482	0.1786

structural fidelity due to the absence of temporal constraints. Excluding the non-rigid pose displacement model introduces additional artifacts, as B-Spline interpolation alone is insufficient to capture complex, high-frequency human motion. Furthermore, model performance declines without the refinement of LBS weights and SMPL shape parameters, underscoring the importance of these optimizations for achieving high-quality results.

Inter-frame regularization loss. We conducted ablation studies on the inter-frame regularization loss \mathcal{L}_{reg} to assess its impact on model performance. The results are presented in Tab. 6 and Fig. 7. Note that results on real data are not included, as ground truth for non-middle timesteps is unavailable. Our findings show that incorporating \mathcal{L}_{reg} significantly enhances model performance, particularly for non-middle timesteps, by enabling more accurate motion sequence direction estimation. Additionally, \mathcal{L}_{reg} provides substantial improvements for middle timesteps for different blur magnitudes, underscoring its essential role in motion estimation and addressing motion-induced blurriness.

Pose interpolation with different control knot numbers. We evaluated our method using various control knot numbers, $P = 2, 3, 4, 5$, for B-Spline sequential pose interpolation. As shown in Tab. 7, our model achieved the best performance with $P = 4$. However, the performance differences were relatively minor. This is due to our non-rigid pose displacement model, which enhances the model with lower P values to handle complex motions more effectively, thereby minimizing performance variation across different control knot numbers.

Impacts of virtual sharp image number. We also examined the impact of different numbers of virtual sharp images $T = 3, 5, 7, 9$. The results, presented in Tab. 7, indicate that the best performance was achieved with $T = 5$.

Ablation results under different blur magnitudes K_{blur} . We also performed ablation studies under different K_{blur} to assess if our method’s design is robust to different blur magnitudes. The results, presented in Tab. 9, indicate the

Table 9. **Quantitative ablation results with different K_{blur} .** We color code result as **best**, **second best**, and **third best**.

K_{blur}	Metrics	w/o interp.	w/o non-rigid	w/o LBS opt.	w/o shape opt.	Ours (full)
7	PSNR \uparrow	23.611	24.813	25.050	25.153	25.155
	SSIM \uparrow	0.7962	0.8127	0.8180	0.8199	0.8200
	LPIPS \downarrow	0.1710	0.1640	0.1563	0.1561	0.1557
9	PSNR \uparrow	22.800	24.239	24.596	24.683	24.680
	SSIM \uparrow	0.7811	0.8035	0.8109	0.8127	0.8126
	LPIPS \downarrow	0.1850	0.1734	0.1638	0.1639	0.1636
11	PSNR \uparrow	22.350	23.754	24.282	24.345	24.353
	SSIM \uparrow	0.7695	0.7924	0.8022	0.8037	0.8039
	LPIPS \downarrow	0.1945	0.1852	0.1725	0.1726	0.1725

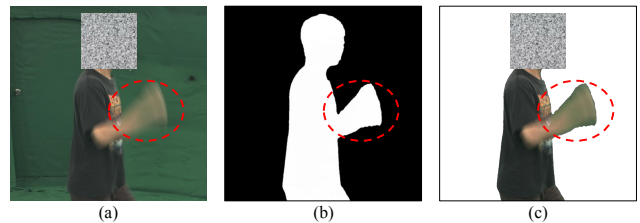


Figure 8. **The limitation of our method.** (a) Captured blurry frame. (b) Pre-computed mask. (c) Body matting according to the mask. Our method do not model the blending effect between human and the background caused by the blur effect, which may harness the performance.

effectiveness of our model components under different blur magnitudes.

5.5. Further Discussions

Results under different blur magnitudes. To assess the robustness of our method across varying levels of blur intensity, we synthesized data with additional blur magnitudes $K_{blur} = 7, 9, 11$. As shown in Tab. 8, the results indicate that performance declines for all methods as K_{blur} increases, which reflects the heightened difficulty associated with more severe blur degradation. Nonetheless, our method consistently surpasses the baseline approaches across all tested levels of blur intensity, demonstrating its resilience and effectiveness under challenging conditions.

Limitations. While our method successfully estimates motion and generates sharp 3DGS human avatars, it has certain limitations. First, as shown in Fig. 8, sub-frame motion can cause blending between the background and the moving foreground (e.g., arms), which does not occur in sharp captures. This blending effect may affect model performance, especially when the background has a significantly higher light intensity than the human subject. Additionally, like other 3DGS avatar methods, our approach depends on pre-computed masks to isolate the human subject from the back-

ground. In future work, we plan to explore adaptive soft mask prediction to overcome these limitations.

6. Conclusion

In this paper, we introduced a novel approach for reconstructing sharp 3D human avatars from blurry video frames. By extending the traditional 2D motion blur process into a 3D-aware blur formation model, our method jointly optimizes sub-frame motion representations while learning a canonical 3DGS human avatar model. To establish a benchmark for this task, we provided a synthetic dataset derived from the ZJU-MoCap dataset and a real-captured dataset acquired using a 360-degree hybrid-exposure camera system. Extensive evaluations demonstrate that our approach outperforms existing baselines.

References

- [1] Easymocap - make human motion capture easier. Github, 2021. 6
- [2] Minh-Quan Viet Bui, Jongmin Park, Jihyong Oh, and Munchurl Kim. Dyblurf: Dynamic deblurring neural radiance fields for blurry monocular video. *arXiv preprint arXiv:2312.13528*, 2023. 2, 3
- [3] Mingdeng Cao, Yanbo Fan, Yong Zhang, Jue Wang, and Yujia Yang. Vdtr: Video deblurring with transformer. *IEEE Transactions on Circuits and Systems for Video Technology*, 33(1):160–171, 2022. 2, 3
- [4] Mingdeng Cao, Zhihang Zhong, Yanbo Fan, Jiahao Wang, Yong Zhang, Jue Wang, Yujia Yang, and Yinqiang Zheng. Towards real-world video deblurring by exploring blur formation process. In *European Conference on Computer Vision*, pages 327–343. Springer, 2022. 1
- [5] Sihun Cha, Kwanggyoon Seo, Amirsaman Ashtari, and Junyong Noh. Generating texture for 3d human avatar from a single image using sampling and refinement networks. In *Computer Graphics Forum*, pages 385–396. Wiley Online Library, 2023. 1
- [6] Jifeng Dai, Haozhi Qi, Yuwen Xiong, Yi Li, Guodong Zhang, Han Hu, and Yichen Wei. Deformable convolutional networks. In *Proceedings of the IEEE international conference on computer vision*, pages 764–773, 2017. 2
- [7] Gerald Farin. *Curves and surfaces for CAD: a practical guide*. Elsevier, 2001. 5
- [8] Chen Geng, Sida Peng, Zhen Xu, Hujun Bao, and Xiaowei Zhou. Learning neural volumetric representations of dynamic humans in minutes. In *Proceedings of the IEEE/CVF Conference on Computer Vision and Pattern Recognition*, pages 8759–8770, 2023. 6
- [9] Chen Guo, Tianjian Jiang, Xu Chen, Jie Song, and Otmar Hilliges. Vid2avatar: 3d avatar reconstruction from videos in the wild via self-supervised scene decomposition. In *Proceedings of the IEEE/CVF Conference on Computer Vision and Pattern Recognition*, pages 12858–12868, 2023. 3
- [10] Liangxiao Hu, Hongwen Zhang, Yuxiang Zhang, Boyao Zhou, Boning Liu, Shengping Zhang, and Liqiang Nie. Gaussianavatar: Towards realistic human avatar modeling from a single video via animatable 3d gaussians. In *Proceedings of the IEEE/CVF Conference on Computer Vision and Pattern Recognition*, pages 634–644, 2024. 1, 3
- [11] Shoukang Hu, Tao Hu, and Ziwei Liu. Gauhuman: Articulated gaussian splatting from monocular human videos. In *Proceedings of the IEEE/CVF Conference on Computer Vision and Pattern Recognition*, pages 20418–20431, 2024. 1, 3, 6, 7
- [12] Yangyi Huang, Hongwei Yi, Yuliang Xiu, Tingting Liao, Jiaxiang Tang, Deng Cai, and Justus Thies. Tech: Text-guided reconstruction of lifelike clothed humans. In *2024 International Conference on 3D Vision (3DV)*, pages 1531–1542. IEEE, 2024. 1
- [13] Zhewei Huang, Tianyuan Zhang, Wen Heng, Boxin Shi, and Shuchang Zhou. Real-time intermediate flow estimation for video frame interpolation. In *European Conference on Computer Vision*, pages 624–642. Springer, 2022. 6
- [14] Tae Hyun Kim and Kyoung Mu Lee. Generalized video deblurring for dynamic scenes. In *Proceedings of the IEEE Conference on Computer Vision and Pattern Recognition*, pages 5426–5434, 2015. 1, 2
- [15] Tae Hyun Kim, Kyoung Mu Lee, Bernhard Scholkopf, and Michael Hirsch. Online video deblurring via dynamic temporal blending network. In *Proceedings of the IEEE international conference on computer vision*, pages 4038–4047, 2017. 1, 2
- [16] Rohit Jena, Ganesh Subramanian Iyer, Siddharth Choudhary, Brandon Smith, Pratik Chaudhari, and James Gee. Splatarmor: Articulated gaussian splatting for animatable humans from monocular rgb videos. *arXiv preprint arXiv:2311.10812*, 2023. 1, 3
- [17] Boyi Jiang, Yang Hong, Hujun Bao, and Juyong Zhang. Selfrecon: Self reconstruction your digital avatar from monocular video. In *Proceedings of the IEEE/CVF Conference on Computer Vision and Pattern Recognition*, pages 5605–5615, 2022. 1
- [18] Tianjian Jiang, Xu Chen, Jie Song, and Otmar Hilliges. Instantavatar: Learning avatars from monocular video in 60 seconds. In *Proceedings of the IEEE/CVF Conference on Computer Vision and Pattern Recognition*, pages 16922–16932, 2023. 3
- [19] Wei Jiang, Kwang Moo Yi, Golnoosh Samei, Oncel Tuzel, and Anurag Ranjan. Neuman: Neural human radiance field from a single video. In *European Conference on Computer Vision*, pages 402–418. Springer, 2022. 1, 3
- [20] Bernhard Kerbl, Georgios Kopanas, Thomas Leimkühler, and George Drettakis. 3d gaussian splatting for real-time radiance field rendering. *ACM Trans. Graph.*, 42(4):139–1, 2023. 1, 2, 3, 7
- [21] Diederik P Kingma and Jimmy Ba. Adam: A method for stochastic optimization. *arXiv preprint arXiv:1412.6980*, 2014. 6
- [22] Alexander Kirillov, Eric Mintun, Nikhila Ravi, Hanzi Mao, Chloe Rolland, Laura Gustafson, Tete Xiao, Spencer Whitehead, Alexander C. Berg, Wan-Yen Lo, Piotr Dollár, and Ross Girshick. Segment anything. *arXiv:2304.02643*, 2023. 6

- [23] Muhammed Kocabas, Jen-Hao Rick Chang, James Gabriel, Oncel Tuzel, and Anurag Ranjan. Hugs: Human gaussian splats. In *Proceedings of the IEEE/CVF conference on computer vision and pattern recognition*, pages 505–515, 2024. 3
- [24] Orest Kupyn, Volodymyr Budzan, Mykola Mykhailych, Dmytro Mishkin, and Jiří Matas. Deblurgan: Blind motion deblurring using conditional adversarial networks. In *Proceedings of the IEEE conference on computer vision and pattern recognition*, pages 8183–8192, 2018. 2
- [25] Orest Kupyn, Tetiana Martyniuk, Junru Wu, and Zhangyang Wang. Deblurgan-v2: Deblurring (orders-of-magnitude) faster and better. In *Proceedings of the IEEE/CVF international conference on computer vision*, pages 8878–8887, 2019. 2
- [26] Dogyoon Lee, Minhyeok Lee, Chajin Shin, and Sangyoun Lee. Dp-nerf: Deblurred neural radiance field with physical scene priors. In *Proceedings of the IEEE/CVF Conference on Computer Vision and Pattern Recognition*, pages 12386–12396, 2023. 2, 3, 7
- [27] Jiahui Lei, Yufu Wang, Georgios Pavlakos, Lingjie Liu, and Kostas Daniilidis. Gart: Gaussian articulated template models. In *Proceedings of the IEEE/CVF Conference on Computer Vision and Pattern Recognition*, pages 19876–19887, 2024. 3
- [28] Anat Levin. Blind motion deblurring using image statistics. *Advances in neural information processing systems*, 19, 2006. 1, 2
- [29] Dasong Li, Xiaoyu Shi, Yi Zhang, Ka Chun Cheung, Simon See, Xiaogang Wang, Hongwei Qin, and Hongsheng Li. A simple baseline for video restoration with grouped spatial-temporal shift. In *Proceedings of the IEEE/CVF Conference on Computer Vision and Pattern Recognition*, pages 9822–9832, 2023. 6, 7
- [30] Moyang Li, Peng Wang, Lingzhe Zhao, Bangyan Liao, and Peidong Liu. Usb-nerf: Unrolling shutter bundle adjusted neural radiance fields. *arXiv preprint arXiv:2310.02687*, 2023. 5
- [31] Ruilong Li, Julian Tanke, Minh Vo, Michael Zollhöfer, Jürgen Gall, Angjoo Kanazawa, and Christoph Lassner. Tava: Template-free animatable volumetric actors. In *European Conference on Computer Vision*, pages 419–436. Springer, 2022. 3
- [32] Zhe Li, Zerong Zheng, Lizhen Wang, and Yebin Liu. Animatable gaussians: Learning pose-dependent gaussian maps for high-fidelity human avatar modeling. In *Proceedings of the IEEE/CVF Conference on Computer Vision and Pattern Recognition*, pages 19711–19722, 2024. 3
- [33] Jingyun Liang, Jiezhong Cao, Guolei Sun, Kai Zhang, Luc Van Gool, and Radu Timofte. Swinir: Image restoration using swin transformer. In *Proceedings of the IEEE/CVF international conference on computer vision*, pages 1833–1844, 2021. 2, 3
- [34] Jingyun Liang, Yuchen Fan, Xiaoyu Xiang, Rakesh Ranjan, Eddy Ilg, Simon Green, Jiezhong Cao, Kai Zhang, Radu Timofte, and Luc V Gool. Recurrent video restoration transformer with guided deformable attention. *Advances in Neural Information Processing Systems*, 35:378–393, 2022. 2, 3, 6, 7
- [35] Jingyun Liang, Jiezhong Cao, Yuchen Fan, Kai Zhang, Rakesh Ranjan, Yawei Li, Radu Timofte, and Luc Van Gool. Vrt: A video restoration transformer. *IEEE Transactions on Image Processing*, 2024. 1, 2, 6, 7
- [36] Tingting Liao, Xiaomei Zhang, Yuliang Xiu, Hongwei Yi, Xudong Liu, Guo-Jun Qi, Yong Zhang, Xuan Wang, Xiangyu Zhu, and Zhen Lei. High-fidelity clothed avatar reconstruction from a single image. In *Proceedings of the IEEE/CVF Conference on Computer Vision and Pattern Recognition*, pages 8662–8672, 2023. 1
- [37] Yang Liu, Xiang Huang, Minghan Qin, Qinwei Lin, and Haoqian Wang. Animatable 3d gaussian: Fast and high-quality reconstruction of multiple human avatars. *arXiv preprint arXiv:2311.16482*, 2023. 3
- [38] Matthew Loper, Naureen Mahmood, Javier Romero, Gerard Pons-Moll, and Michael J Black. Smpl: A skinned multi-person linear model. In *Seminal Graphics Papers: Pushing the Boundaries, Volume 2*, pages 851–866. 2023. 1, 2, 3, 4, 5
- [39] Li Ma, Xiaoyu Li, Jing Liao, Qi Zhang, Xuan Wang, Jue Wang, and Pedro V Sander. Deblur-nerf: Neural radiance fields from blurry images. In *Proceedings of the IEEE/CVF Conference on Computer Vision and Pattern Recognition*, pages 12861–12870, 2022. 2, 3, 7
- [40] Ben Mildenhall, Pratul P Srinivasan, Matthew Tancik, Jonathan T Barron, Ravi Ramamoorthi, and Ren Ng. Nerf: Representing scenes as neural radiance fields for view synthesis. *Communications of the ACM*, 65(1):99–106, 2021. 2, 3
- [41] Arthur Moreau, Jifei Song, Helisa Dharmo, Richard Shaw, Yiren Zhou, and Eduardo Pérez-Pellitero. Human gaussian splatting: Real-time rendering of animatable avatars. In *Proceedings of the IEEE/CVF Conference on Computer Vision and Pattern Recognition*, pages 788–798, 2024. 3
- [42] Seungjun Nah, Tae Hyun Kim, and Kyoung Mu Lee. Deep multi-scale convolutional neural network for dynamic scene deblurring. In *Proceedings of the IEEE conference on computer vision and pattern recognition*, pages 3883–3891, 2017. 1, 2
- [43] Seungjun Nah, Sanghyun Son, and Kyoung Mu Lee. Recurrent neural networks with intra-frame iterations for video deblurring. In *Proceedings of the IEEE/CVF conference on computer vision and pattern recognition*, pages 8102–8111, 2019. 1, 2
- [44] Atsuhiko Noguchi, Xiao Sun, Stephen Lin, and Tatsuya Harada. Neural articulated radiance field. In *Proceedings of the IEEE/CVF International Conference on Computer Vision*, pages 5762–5772, 2021. 1, 3
- [45] Jinshan Pan, Haoran Bai, and Jinhui Tang. Cascaded deep video deblurring using temporal sharpness prior. In *Proceedings of the IEEE/CVF conference on computer vision and pattern recognition*, pages 3043–3051, 2020. 2
- [46] Jinshan Pan, Boming Xu, Jiangxin Dong, Jianjun Ge, and Jinhui Tang. Deep discriminative spatial and temporal network for efficient video deblurring. In *Proceedings of*

- the IEEE/CVF Conference on Computer Vision and Pattern Recognition*, pages 22191–22200, 2023. 2
- [47] Juraj Parajka, Peter Haas, Robert Kirnbauer, Josef Jansa, and Günter Blöschl. Potential of time-lapse photography of snow for hydrological purposes at the small catchment scale. *Hydrological Processes*, 26(22):3327–3337, 2012. 1
- [48] Adam Paszke, Sam Gross, Francisco Massa, Adam Lerer, James Bradbury, Gregory Chanan, Trevor Killeen, Zeming Lin, Natalia Gimelshein, Luca Antiga, et al. Pytorch: An imperative style, high-performance deep learning library. *Advances in neural information processing systems*, 32, 2019. 6
- [49] Sida Peng, Junting Dong, Qianqian Wang, Shangzhan Zhang, Qing Shuai, Xiaowei Zhou, and Hujun Bao. Animatable neural radiance fields for modeling dynamic human bodies. In *Proceedings of the IEEE/CVF International Conference on Computer Vision*, pages 14314–14323, 2021. 3
- [50] Sida Peng, Yuanqing Zhang, Yinghao Xu, Qianqian Wang, Qing Shuai, Hujun Bao, and Xiaowei Zhou. Neural body: Implicit neural representations with structured latent codes for novel view synthesis of dynamic humans. In *Proceedings of the IEEE/CVF Conference on Computer Vision and Pattern Recognition*, pages 9054–9063, 2021. 1, 2, 6
- [51] Sida Peng, Shangzhan Zhang, Zhen Xu, Chen Geng, Boyi Jiang, Hujun Bao, and Xiaowei Zhou. Animatable neural implicit surfaces for creating avatars from videos. *arXiv preprint arXiv:2203.08133*, 4(5), 2022. 3
- [52] Zhiyin Qian, Shaofei Wang, Marko Mihajlovic, Andreas Geiger, and Siyu Tang. 3dgs-avatar: Animatable avatars via deformable 3d gaussian splatting. In *Proceedings of the IEEE/CVF Conference on Computer Vision and Pattern Recognition*, pages 5020–5030, 2024. 1, 3, 6
- [53] Kaihuai Qin. General matrix representations for b-splines. In *Proceedings Pacific Graphics’ 98. Sixth Pacific Conference on Computer Graphics and Applications (Cat. No. 98EX208)*, pages 37–43. IEEE, 1998. 5
- [54] Wenqi Ren, Jinshan Pan, Xiaochun Cao, and Ming-Hsuan Yang. Video deblurring via semantic segmentation and pixel-wise non-linear kernel. In *Proceedings of the IEEE International Conference on Computer Vision*, pages 1077–1085, 2017. 1, 2
- [55] Michael Rubinstein, Ce Liu, Peter Sand, Fredo Durand, and William T Freeman. Motion denoising with application to time-lapse photography. In *CVPR 2011*, pages 313–320. IEEE, 2011. 1
- [56] Hyeonseok Son, Junyong Lee, Jonghyeop Lee, Sunghyun Cho, and Seungyong Lee. Recurrent video deblurring with blur-invariant motion estimation and pixel volumes. *ACM Transactions on Graphics (TOG)*, 40(5):1–18, 2021. 2
- [57] Colton Stearns, Adam Harley, Mikaela Uy, Florian Dubost, Federico Tombari, Gordon Wetzstein, and Leonidas Guibas. Dynamic gaussian marbles for novel view synthesis of casual monocular videos. *arXiv preprint arXiv:2406.18717*, 2024. 2, 3
- [58] Shuochen Su, Mauricio Delbracio, Jue Wang, Guillermo Sapiro, Wolfgang Heidrich, and Oliver Wang. Deep video deblurring for hand-held cameras. In *Proceedings of the IEEE conference on computer vision and pattern recognition*, pages 1279–1288, 2017. 1, 2
- [59] Shih-Yang Su, Frank Yu, Michael Zollhöfer, and Helge Rhodin. A-nerf: Articulated neural radiance fields for learning human shape, appearance, and pose. *Advances in neural information processing systems*, 34:12278–12291, 2021. 1, 3
- [60] Huiqiang Sun, Xingyi Li, Liao Shen, Xinyi Ye, Ke Xian, and Zhiguo Cao. Dyblurf: Dynamic neural radiance fields from blurry monocular video. In *Proceedings of the IEEE/CVF Conference on Computer Vision and Pattern Recognition*, pages 7517–7527, 2024. 2, 3
- [61] Xin Tao, Hongyun Gao, Xiaoyong Shen, Jue Wang, and Ji-aya Jia. Scale-recurrent network for deep image deblurring. In *Proceedings of the IEEE conference on computer vision and pattern recognition*, pages 8174–8182, 2018. 1, 2
- [62] Michael Unser, Akram Aldroubi, and Murray Eden. B-spline signal processing. i. theory. *IEEE transactions on signal processing*, 41(2):821–833, 1993. 5
- [63] Peng Wang, Lingzhe Zhao, Ruijie Ma, and Peidong Liu. Bad-nerf: Bundle adjusted deblur neural radiance fields. In *Proceedings of the IEEE/CVF Conference on Computer Vision and Pattern Recognition*, pages 4170–4179, 2023. 2, 3, 7
- [64] Shaofei Wang, Katja Schwarz, Andreas Geiger, and Siyu Tang. Arah: Animatable volume rendering of articulated human sdf. In *European conference on computer vision*, pages 1–19. Springer, 2022. 1, 3
- [65] Xintao Wang, Kelvin CK Chan, Ke Yu, Chao Dong, and Chen Change Loy. Edvr: Video restoration with enhanced deformable convolutional networks. In *Proceedings of the IEEE/CVF conference on computer vision and pattern recognition workshops*, pages 0–0, 2019. 1, 2
- [66] Yusheng Wang, Yunfan Lu, Ye Gao, Lin Wang, Zhihang Zhong, Yinqiang Zheng, and Atsushi Yamashita. Efficient video deblurring guided by motion magnitude. In *European Conference on Computer Vision*, pages 413–429. Springer, 2022. 1, 2
- [67] Chung-Yi Weng, Brian Curless, Pratul P Srinivasan, Jonathan T Barron, and Ira Kemelmacher-Shlizerman. Humannerf: Free-viewpoint rendering of moving people from monocular video. In *Proceedings of the IEEE/CVF conference on computer vision and pattern Recognition*, pages 16210–16220, 2022. 1, 3, 6
- [68] Jonas Wulff and Michael Julian Black. Modeling blurred video with layers. In *Computer Vision—ECCV 2014: 13th European Conference, Zurich, Switzerland, September 6–12, 2014, Proceedings, Part VI 13*, pages 236–252. Springer, 2014. 1, 2
- [69] Hongyi Xu, Thiemo Alldieck, and Cristian Sminchisescu. H-nerf: Neural radiance fields for rendering and temporal reconstruction of humans in motion. *Advances in Neural Information Processing Systems*, 34:14955–14966, 2021. 1, 3
- [70] Keyang Ye, Tianjia Shao, and Kun Zhou. Animatable 3d gaussians for high-fidelity synthesis of human motions. *arXiv preprint arXiv:2311.13404*, 2023. 3

- [71] Zhengming Yu, Wei Cheng, Xian Liu, Wayne Wu, and Kwan-Yee Lin. Monohuman: Animatable human neural field from monocular video. In *Proceedings of the IEEE/CVF Conference on Computer Vision and Pattern Recognition*, pages 16943–16953, 2023. [3](#)
- [72] Syed Waqas Zamir, Aditya Arora, Salman Khan, Munawar Hayat, Fahad Shahbaz Khan, Ming-Hsuan Yang, and Ling Shao. Multi-stage progressive image restoration. In *Proceedings of the IEEE/CVF conference on computer vision and pattern recognition*, pages 14821–14831, 2021. [1](#), [2](#)
- [73] Syed Waqas Zamir, Aditya Arora, Salman Khan, Munawar Hayat, Fahad Shahbaz Khan, and Ming-Hsuan Yang. Restormer: Efficient transformer for high-resolution image restoration. In *Proceedings of the IEEE/CVF conference on computer vision and pattern recognition*, pages 5728–5739, 2022. [2](#), [3](#)
- [74] Huicong Zhang, Haozhe Xie, and Hongxun Yao. Blur-aware spatio-temporal sparse transformer for video deblurring. In *Proceedings of the IEEE/CVF Conference on Computer Vision and Pattern Recognition*, pages 2673–2681, 2024. [6](#), [7](#)
- [75] Jingbo Zhang, Xiaoyu Li, Qi Zhang, Yanpei Cao, Ying Shan, and Jing Liao. Humanref: Single image to 3d human generation via reference-guided diffusion. In *Proceedings of the IEEE/CVF Conference on Computer Vision and Pattern Recognition*, pages 1844–1854, 2024. [1](#)
- [76] Lingzhe Zhao, Peng Wang, and Peidong Liu. Bad-gaussians: Bundle adjusted deblur gaussian splatting. *arXiv preprint arXiv:2403.11831*, 2024. [2](#), [3](#), [7](#)
- [77] Zhihang Zhong, Ye Gao, Yinqiang Zheng, and Bo Zheng. Efficient spatio-temporal recurrent neural network for video deblurring. In *Computer Vision—ECCV 2020: 16th European Conference, Glasgow, UK, August 23–28, 2020, Proceedings, Part VI 16*, pages 191–207. Springer, 2020. [1](#), [2](#)
- [78] Zhihang Zhong, Xiao Sun, Zhirong Wu, Yinqiang Zheng, Stephen Lin, and Imari Sato. Animation from blur: Multi-modal blur decomposition with motion guidance. In *European Conference on Computer Vision*, pages 599–615. Springer, 2022.
- [79] Zhihang Zhong, Mingdeng Cao, Xiang Ji, Yinqiang Zheng, and Imari Sato. Blur interpolation transformer for real-world motion from blur. In *Proceedings of the IEEE/CVF Conference on Computer Vision and Pattern Recognition*, pages 5713–5723, 2023. [2](#)
- [80] Shangchen Zhou, Jiawei Zhang, Jinshan Pan, Haozhe Xie, Wangmeng Zuo, and Jimmy Ren. Spatio-temporal filter adaptive network for video deblurring. In *Proceedings of the IEEE/CVF international conference on computer vision*, pages 2482–2491, 2019. [1](#), [2](#)
- [81] Xizhou Zhu, Han Hu, Stephen Lin, and Jifeng Dai. Deformable convnets v2: More deformable, better results. In *Proceedings of the IEEE/CVF conference on computer vision and pattern recognition*, pages 9308–9316, 2019. [2](#)
- [82] Wojciech Zielonka, Timur Bagautdinov, Shunsuke Saito, Michael Zollhöfer, Justus Thies, and Javier Romero. Drivable 3d gaussian avatars. *arXiv preprint arXiv:2311.08581*, 2023. [3](#)